Computers and Structures 284 (2023) 107069

Contents lists available at ScienceDirect

Computers and Structures

journal homepage: www.elsevier.com/locate/compstruc

Fail-safe topology optimization for multiscale structures

Jianghong Yang [a], Hailiang Su [b], Xinqing Li [a], Yingjun Wang [a,c,*]

[a] National Engineering Research Center of Novel Equipment for Polymer Processing, The Key Laboratory of Polymer Processing Engineering of the Ministry of Education, Guangdong Provincial Key Laboratory of Technique and Equipment for Macromolecular Advanced Manufacturing, South China University of Technology, Guangzhou 510641, China
[b] School of Mechanical and Automotive Engineering, Guangxi University of Science and Technology, Liuzhou 545006, China
[c] State Key Laboratory of Digital Manufacturing Equipment and Technology, Huazhong University of Science and Technology, Wuhan 430074, China

ARTICLE INFO

Article history:
Received 8 December 2022
Accepted 4 May 2023
Available online 16 May 2023

Keywords:
Fail-safe topology optimization
Multiscale structures
Partial damage
Homogenization method
Heaviside projection

ABSTRACT

This paper presents a novel fail-safe topology optimization method for multiscale structures. The partial damage of both macroscopic and microscopic scales is considered for structural design. To ensure precision, the effective elasticity tensor obtained by the homogenization method is fitted as a high-order polynomial function. Meanwhile, the simplified models of partially damaged truss-like microstructure are employed to reduce the computational cost and the difficulty of fitting. Moreover, Heaviside projection is applied to speed up the convergence and yield a relatively clear configuration. Three numerical examples are tested to demonstrate that the optimized multiscale structures successfully obtain comprehensive performances than optimized solid structures when appropriate microstructure configurations are chosen. Besides, multiscale structures are more self-supporting than solid structures and thus more suitable for additive manufacturing due to the large number of gray elements diffused.

1. Introduction

Topology optimization (TO) is becoming an important method in structural design with increasing computational power of computers. Especially since the pioneering work of Bendsøe and Kikuchi [1], the homogenization method (HM) was adopted to achieve continuum structural TO. Since then, many remarkable TO methods were presented. The solid isotropic material with penalization (SIMP) as a simple and efficient method [2,3] has been widely used in TO since it was presented. The TO based on level-set method [4,5] which utilizes level-set function to implicitly describe the structural geometries during TO can obtain clear topological boundaries. The TO based on moving morphable components (MMC) [6,7], whose number of design variables depends on the number of components, has received extensive attention.

The traditional TO design usually seeks the optimal mechanical properties during normal working conditions, which is easily unstable when encounters failure due to its low redundancy. Thus, using such a structure is very dangerous when it is subjected to damage. In civil engineering, mechanical engineering and aerospace engineering, the redundant design runs through the entire design process. Sun et al. [8] applied the fail-safe concept to the design of the truss structure. In their numerical examples, the damage of a single truss and a group of trusses were considered respectively, and the multi-constraint optimization problems were solved under these conditions. Lüdeker and Kriegesmann [9] explored the feasibility of combining damage scenarios. The resulting structure may be unsafe when encountering a single damage scenario, but applying the p-norm to stress constraints can reduce this effect. In addition, a series of articles have also investigated the fail-safe optimization of truss structures, e.g. [10–13].

Jansen et al. [14] first extended the fail-safe concept to continuum structural TO. They specified the size of the damage patch and then applied the damage at all feasible locations. Such a design can withstand damage from various locations, but this method brings computational challenges. Based on this problem, Zhou and Fleury [15] reduced the amount of damage scenarios in each iteration by controlling the distance between every two adjacent damage areas. And they ultimately implemented a fail-safe TO (FSTO) for a 3D vehicle control arm model. To further reduce the computational cost, Ambrozkiewicz and Kriegesmann [16,17] presented the stress criterion and image processing for identifying the beams and knots of the structures where the damage was applied. Hederberg and Thore [18] employed the MMC to apply damage, and components were used to erase material whose locations were determined by the inner maximization compliance problem, which is similar to

* Corresponding author at: National Engineering Research Center of Novel Equipment for Polymer Processing, The Key Laboratory of Polymer Processing Engineering of the Ministry of Education, Guangdong Provincial Key Laboratory of Technique and Equipment for Macromolecular Advanced Manufacturing, South China University of Technology, Guangzhou 510641, China.

E-mail address: wangyj84@scut.edu.cn (Y. Wang).

https://doi.org/10.1016/j.compstruc.2023.107069
0045-7949/

the approach presented by Ambrozkiewicz and Kriegesmann [17]. In Martínez-Frutos and Ortigosa [19], the probability of damage occurrence and the uncertainty of damage patch size are taken into account during the design process, thus a less costly design with known risks is obtained. It is worth mentioning that the above-mentioned failures do not take into account the gradual propagation of damage, which is a focus in other papers. More details can be found in [20–23].

Current FSTO focus on changing the configuration of the macrostructure to increase its robustness. Another powerful approach to achieve it is reinforcing the strength of the material. One effective approach is to fill the structure with microstructure cells, i.e., to design the multiscale structures. Thus an extreme performance structure can be designed, which is difficult to achieve by solid structures [24–27]. Qiu et al. [28] compared the mechanical properties of optimized multiscale structures and optimized solid structures after encountering the same damage. On an equal-mass basis, the optimized multiscale structures had lower compliance and maximum stress than the solid structures. Do et al. [29] utilized infill optimization [30] to generate the redundant structure, and then filled it with four kinds of microstructure unit cells. By comparing the max displacement of these structures after applying the same damage scenarios, they found that the Voronoi cellular structure was the most robust one among them. However, the multiscale structures mentioned above are not designed with the concept of fail-safe. Inspired by these, this paper will implement the multiscale FSTO (MFSTO) and demonstrate the advantages of such multiscale structures. The HM that is widely used in multiscale TO [31] and microstructure design [32] will be also adopted to calculate the equivalent properties of the microstructures.

The remainder of this paper is as follows: Section 2 analyzes and simplifies the partial damage of multiscale structures. Section 3 presents a FSTO problem and briefly introduces SIMP and HM, as well as the associated mathematical model. Section 4 elaborates on the algorithm implementation and analyzes the sensitivity of the MFSTO. In Section 5, both 2D and 3D examples are tested to illustrate the effectiveness of the algorithm and demonstrate the superiority of the optimized multiscale structures. Conclusions and future works are given in Section 6.

2. Simplified method for partial damage of multiscale structures

Describing damage to a structure is a significant part of FSTO. The approach of Zhou and Fleury [15] considering the damage is representative. They first specified the size of the damage patch. To reduce the computational cost, they divided failure set into levels according to the number of considered failure scenarios. In the damage set of level 1 (PA1), the damage patches fill the design domain without overlapping. Moreover, the damage set of level 2 (PA2) can be obtained by halving the distance of adjacent damage patches in the level 1 damage set.

The utilization of simplifying damage models can effectively reduce computational costs. Take Fig. 1 as an example, an elliptic damage is applied to the solid structure and the multiscale structure, respectively. The way of simplifying the damage to a solid structure in [17,18] is shown in Fig. 1(a). After describing the damage patch by the level-set function, the level-set values at the elements' positions are substituted into the Heaviside function to obtain their densities. The way simplifies the damage to a multiscale structure is quite different in this paper. Since the damaged microstructure still has some supporting capacity under some failure modes, the damage inside the microstructure is considered in this paper. As represented in Fig. 1(b), the entirely removed element will be assigned a very low density. While the partially damaged element will be given an intermediate density, and HM will be applied to obtain its mechanical properties. However, since the mechanical properties of the damaged graded material are usually complex to fit as a function of density, simplified models are used in this paper. As shown on the right of Fig. 1(b), the truss-like damaged microstructure is simplified via removing trusses covered with the failure area, which is inspired by the method in fail-safe optimization of truss structures. Meanwhile, the computational cost of pre-processing is also reduced due to the complex damaged model can be simplified into a few specific kinds.

In the following examples, the abovementioned method will be used to simplify damage of multiscale structure, and the damage set division approach will be employed to reduce the computational cost.

3. FSTO problem for multiscale structures

A FSTO problem can be formulated by Eq. (1), where the design variables are the element densities, the objective function is to minimize the maximum compliance of all failure scenarios, and the constraint is the volume fraction:

$$\begin{cases} \text{find}: \boldsymbol{\rho} = \{\rho_1, \rho_2, \ldots, \rho_n\}^{\mathrm{T}} \\ \min: J(\boldsymbol{\rho}) = \max\{c^{(i)}(\boldsymbol{\rho})\} \;\; i = 1, 2, \ldots, m \\ \text{s.t.} \;\; \frac{V(\boldsymbol{\rho})}{V_0} \leqslant f_0 \\ \rho_{\min} \leqslant \rho_j \leqslant \rho_{\max} \;\; j = 1, 2, \ldots, n \end{cases} \tag{1}$$

where $\boldsymbol{\rho}$ indicates the density vector; n represents the number of elements; $c^{(i)}(\boldsymbol{\rho})$ is the structural compliance when it encounters the ith failure scenario; $J(\boldsymbol{\rho})$ is the objective function which is equal to the maximum compliance for all m failure scenarios; $V(\boldsymbol{\rho})$ and V_0 represent the volume of material and the design domain, respectively; f_0 is the global volume constraint.

In the gradient-based optimization algorithm, it is necessary to obtain the sensitivity of the objective function. But the maximum function is indifferentiable, hence, the K-S function [33] is often used to approximate the maximum function. The objective function can be replaced by the following formula:

$$\bar{J}(\boldsymbol{\rho}) = \frac{1}{\gamma} \ln \sum_{i=1}^{m} e^{\gamma c^{(i)}(\boldsymbol{\rho})} \tag{2}$$

where the larger value when γ is set, the closer the value of the K-S function is to the maximum value, but it may result in the numerical unstable. According to [14], $\gamma = 50/\max\{c^{(i)}(\boldsymbol{\rho})\}$ $(i = 1, 2, \ldots, m)$ is a suitable choice in the algorithm.

Assuming that the structure is in the ith damage scenario, now the nodal displacement vector is $\boldsymbol{u}^{(i)}$, and the global stiffness matrix is $\boldsymbol{K}^{(i)}$, then the compliance of the damaged structure can be obtained by $c^{(i)}(\boldsymbol{\rho}) = \boldsymbol{f}^{T}\boldsymbol{u}^{(i)} = (\boldsymbol{u}^{(i)})^{\mathrm{T}}\boldsymbol{K}^{(i)}\boldsymbol{u}^{(i)}$. In finite element analysis (FEA), the global stiffness matrix $\boldsymbol{K}$ is assembled from the element stiffness matrix $\boldsymbol{K}_E$.

For solid structures, the SIMP method is usually utilized to describe the material properties. The element stiffness matrix $\boldsymbol{K}_E$ for the element with density ρ can be obtained as:

$$\boldsymbol{K}_E = [E_{\min} + \rho^p (E_0 - E_{min})]\boldsymbol{K}_0 \tag{3}$$

where E_0 and v_0 are the Young's modulus and Poisson's ratio of the solid material, respectively; $E_{\min}$ is the Young's modulus of the void material; p denotes the penalization parameter to favor 0–1 solutions and $p = 3$ is a typical choice [34]; $\boldsymbol{K}_0$ is the element stiffness matrix for an element with unit Young's modulus.

For multiscale structures, the mechanical properties of microstructure at the macroscopic scale can be accessed via HM.

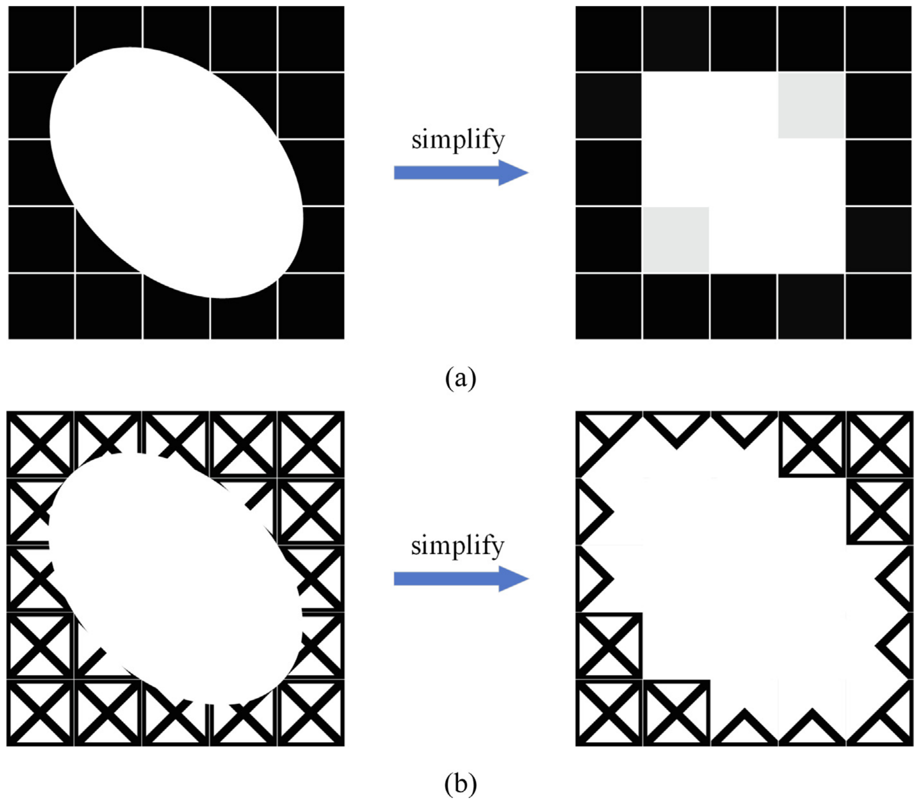

Fig. 1. Two structures encounter elliptic damage and simplify methods for (a) damage of solid structure in [17,18] and (b) damage of multiscale structure.

If x and y are variables on the macroscopic and microscopic scale respectively, they satisfy the following relationship, where $0 < \varepsilon \ll 1$:

$$y = \frac{x}{\varepsilon} \tag{4}$$

The displacement field u can be expanded by ε:

$$u(x, y) = u_0(x, y) + \varepsilon u_1(x, y) + \varepsilon^2 u_2(x, y) + \ldots \tag{5}$$

Besides, the effective elasticity tensor D_{ijkl}^H can be calculated as:

$$D_{ijkl}^H = \frac{1}{|Y|} \int_Y \left(\varepsilon_{pq}^0(u_{ij}) - \varepsilon_{pq}(u_{ij}) \right) D_{pqrs} \left(\varepsilon_{rs}^0(u_{kl}) - \varepsilon_{rs}(u_{kl}) \right) dY \tag{6}$$

where Y is the design domain of the microstructure, D_{pqrs} is the elasticity tensor of the filling material, $\varepsilon_{pq}^0(u_{ij})$ is the unit test strain field, $\varepsilon_{pq}(u_{ij})$ is the strain field which can be gained from the following formula:

$$\int_Y \varepsilon_{pq}(u_{ij}) D_{pqrs} \varepsilon_{rs}(v_{kl}) dY = \int_Y \varepsilon_{pq}^0(u_{ij}) D_{pqrs} \varepsilon_{rs}(v_{kl}) dY, \forall v_{kl} \in \bar{\boldsymbol{U}}(Y) \tag{7}$$

where $\bar{\boldsymbol{U}}(Y)$ represents the admissible displacement field defined in Y.

After each effective elasticity tensor D_{ijkl}^H is obtained, it can be written as a matrix $\boldsymbol{D}^H$ whose sizes are 3×3 in the 2D case and 6×6 in the 3D case, respectively. The element stiffness matrix $\boldsymbol{K}_E$ can be obtained by the following formula:

$$\boldsymbol{K}_E = \int_Y \boldsymbol{B}_e^T \boldsymbol{D} \boldsymbol{B}_e \mathrm{d}Y \tag{8}$$

where $\boldsymbol{B}_e$ denotes the strain–displacement matrix.

Although $\boldsymbol{K}_E$ for a microstructure element can be calculated, the HM is complex and time-consuming. Therefore, to improve the computational cost, the effective elasticity tensor $\boldsymbol{D}_{ijkl}^H$ is fitted to a function of the density ρ, which is generally a polynomial. In this way, the effective elastic tensor and its sensitivity can be directly obtained.

4. Sensitivity analysis of MFSTO

Replacing the objective function in Eq. (1) with Eq. (2) turns the optimization problem into:

$$\begin{cases} \text{find} : \boldsymbol{\rho} = \{\rho_1, \rho_2, \ldots, \rho_n\}^{\mathrm{T}} \\ \min : \bar{J}(\boldsymbol{\rho}) = \frac{1}{\gamma} \ln \sum_{i=1}^{m} e^{\gamma c^{(i)}(\boldsymbol{\rho})} \; i = 1, 2, \ldots, m \\ \text{s.t.} \quad \frac{V(\boldsymbol{\rho})}{V_0} \leqslant f_0 \\ \rho_{\min} \leqslant \rho_j \leqslant \rho_{\max} \; j = 1, 2, \ldots, n \end{cases} \tag{9}$$

This optimization problem can be solved through the method of moving asymptotes (MMA) [35,36]. For the MMA solver, it is compulsory to find the sensitivity of the objective function and the constraint function.

4.1. Density filter and projection

The following filter is adopted to attain smoother designs and avoid check-board pattern [37]:

$$\tilde{\rho}_i = \frac{\sum_{h=1}^{n} w_{ih} v_h \rho_h}{\sum_{h=1}^{n} w_{ih} v_h} \tag{10}$$

$$w_{ih} = \max\left\{0, R_{\min} - \| \boldsymbol{x}_i - \boldsymbol{x}_h \|_2 \right\} \tag{11}$$

where $\widetilde{\rho}_i$ is the density of element i after filtering; w_{ih} is the weight factor which is related to the distance between element i and h; v_h is the volume of element h; $R_{\min}$ is the filtering radius; $\| \boldsymbol{x}_i - \boldsymbol{x}_h \|_2$ represents elemental center distance.

To obtain clearer 0–1 solutions, the Heaviside step function [38] is employed as the density projection:

$$\bar{\rho}_i = \frac{\tanh(\beta\eta) + \tanh(\beta(\widetilde{\rho}_i - \eta))}{\tanh(\beta\eta) + \tanh(\beta(1-\eta))} \tag{12}$$

where β is referred to the steepness parameter, which determines the strength of the projection; $\eta \in [0, 1]$ is the projection threshold, values higher than η will be projected to 1 and values less than η will be projected to 0.

Their sensitivities can be obtained as:

$$\frac{\partial \widetilde{\rho}_i}{\partial \rho_j} = \frac{w_{ij} v_j}{\sum_{h=1}^{n} w_{ih} v_h} \tag{13}$$

$$\frac{\partial \bar{\rho}_i}{\partial \widetilde{\rho}_i} = \frac{\beta\left[1 - \tanh^2(\beta(\widetilde{\rho}_i - \eta))\right]}{\tanh(\beta\eta) + \tanh(\beta(1-\eta))} \tag{14}$$

4.2. The description of the failure and the related sensitivity

Generally, in FSTO, assigning an element a very small density indicates that this element is damaged. It can be expressed as:

$$\bar{\boldsymbol{\rho}}^{(k)} = \boldsymbol{\phi}^{(k)} \circ \bar{\boldsymbol{\rho}} \tag{15}$$

where $\bar{\boldsymbol{\rho}}^{(k)}$ is the density vector when the structure is in the kth failure scenario; $\boldsymbol{\phi}^{(k)}$ denotes the damage mask of the kth failure scenario which is a matrix with a value of $[0, 1]$, where 0 and 1 denote that the element is completely removed and completely reserved respectively, and an intermediate value means that the element is partially removed; $\circ$ represents the Hadamard product.

When the damage mask is independent of the density, for example, the solid element encounters damage or the failure will not change the configuration of the microstructural element, the sensitivity does not require additional calculations:

$$\frac{\partial \bar{\rho}_i^{(k)}}{\partial \bar{\rho}_i} = \phi_i^{(k)} \tag{16}$$

If damage mask is dependent of density, e.g. the configuration of the microstructural element is changed after damage, the sensitivity should be computed according to the specific failure scenario. In the situation displayed in Fig. 2, it is assumed that the truss-like element i suffers different local damages in the jth and kth damage scenarios, respectively. Although the relative density and elasticity matrix of the microstructure changed after failure, the rod diameter does not change, which can be used as an intermediate variable to obtain the relative density after failure and the sensitivity of the densities.

Taking the kth failure scenario as an example, if the relationship between the relative density $\bar{\rho}_i$ of the microstructure and the rod diameter d is $\bar{\rho}_i = s(d)$, and the relationship between the relative density of the damaged microstructure $\bar{\rho}_i^{(k)}$ and the rod diameter d is $\bar{\rho}_i^{(k)} = s^{(k)}(d)$, $\bar{\rho}_i^{(k)}$ can be obtained by following:

$$\bar{\rho}_i^{(k)} = s^{(k)}\left(s^{-1}\left(\bar{\rho}_i\right)\right) \tag{17}$$

where $d = s^{-1}\left(\bar{\rho}_i\right)$ and $\bar{\rho}_i = s(d)$ are inverse functions for each other.

If both of them are one-dimensional functions of the rod diameter d, the sensitivity of this part can be obtained by the following formula:

$$\frac{\partial \bar{\rho}_i^{(k)}}{\partial \bar{\rho}_i} = \frac{\partial \bar{\rho}_i^{(k)}}{\partial d} \frac{\partial d}{\partial \bar{\rho}_i} = \frac{\partial \bar{\rho}_i^{(k)}}{\partial d} \Big/ \frac{\partial \bar{\rho}_i}{\partial d} = \frac{s^{(k)'}(d)}{s'(d)} \tag{18}$$

Since $s(d)$ and $s^{(k)}(d)$ are sometimes difficult to obtain, the effective elasticity matrix $\boldsymbol{D}_i^{H(k)}$ of the damaged element can be fitted as a function of $\bar{\rho}_i$. Therefore $\partial \boldsymbol{D}_i^{H(k)} / \partial \bar{\rho}_i$ can be calculated and $\partial \bar{\rho}_i^{(k)} / \partial \bar{\rho}_i$ is no longer needed at this time. But the relationship curve obtained in this way is often not smooth and difficult to fit. Using the simplified damage model can reduce the difficulty of calculating $s^{(k)}(d)$.

4.3. Compliance and its sensitivity

When considering the kth failure scenario, the effective elasticity matrix $\boldsymbol{D}_i^{H(k)}$ of element i can be obtained by the HM. Substituting $\boldsymbol{D}_i^{(k)}$ into Eq. (8) to obtain the element stiffness matrix of element i, i.e. $\boldsymbol{K}_{Ei}^{(k)}$, then the compliance of element i can be obtained as:

$$c_i^{(k)} = \left(\boldsymbol{u}_i^{(k)}\right)^{\mathrm{T}} \boldsymbol{K}_{Ei}^{(k)} \boldsymbol{u}_i^{(k)} \tag{19}$$

where $\boldsymbol{u}_i^{(k)}$ is the displacement vector of element i. Subsequently, the structural compliance $c^{(k)}$ can be achieved by accumulating:

$$c^{(k)} = \sum_{h=1}^{n} c_h^{(k)} \tag{20}$$

Since the compliance of element i is independent of other elements' densities, the partial derivative of the compliance $c^{(k)}$ with respect to $\bar{\rho}_j^{(k)}$ is formulated as:

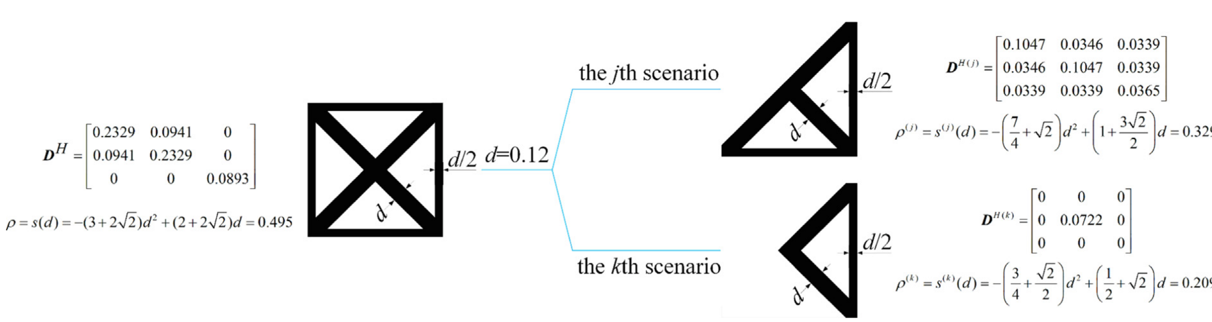

Fig. 2. The truss-like microstructure encounters partial failure.

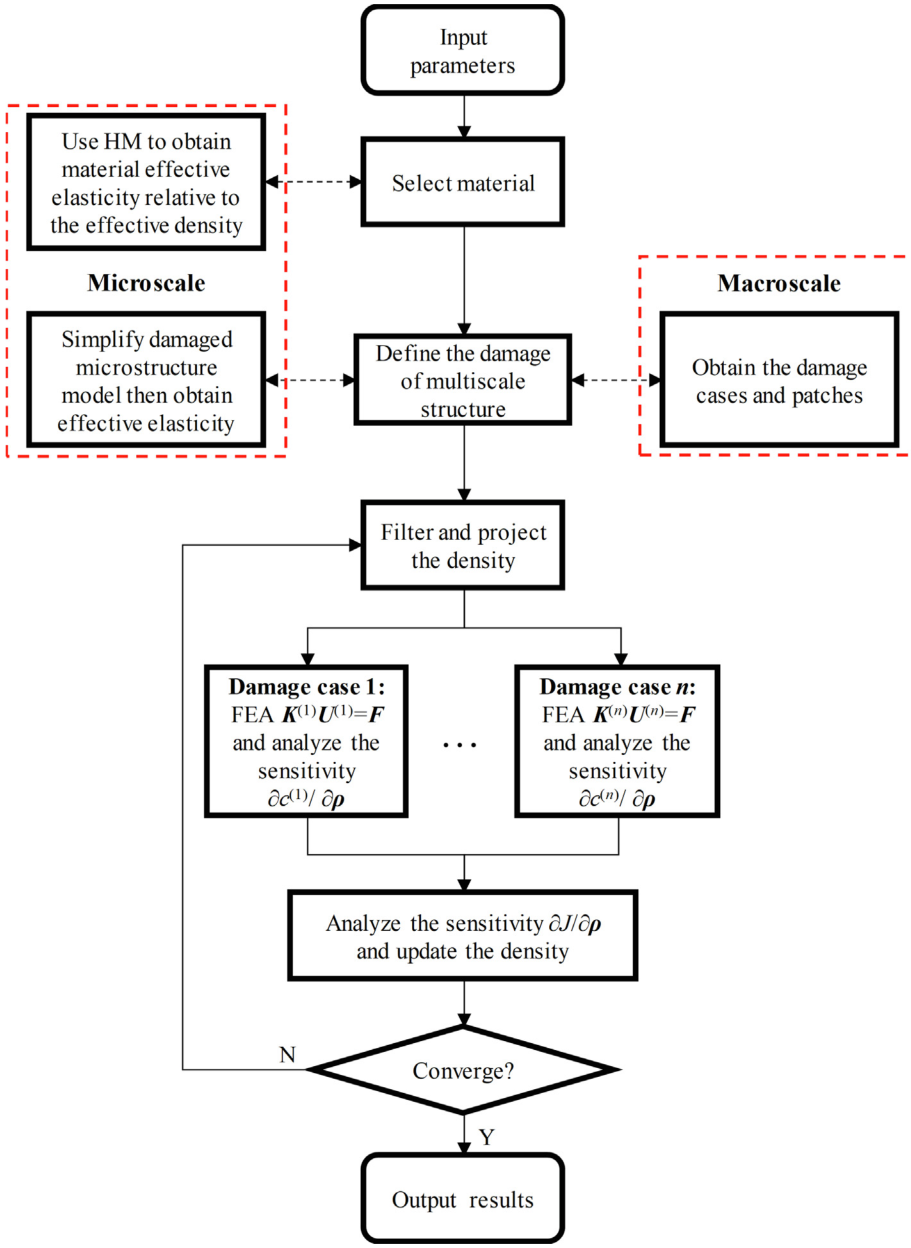

Fig. 3. The flow chart of MFSTO.

$$\frac{\partial c^{(k)}}{\partial \bar{\rho}_i^{(k)}} = \frac{\partial c_i^{(k)}}{\partial \bar{\rho}_i^{(k)}} = -\left(\boldsymbol{u}_i^{(k)}\right)^{\mathrm{T}} \cdot \frac{\partial \boldsymbol{K}_{Ei}^{(k)}}{\partial \bar{\rho}_i^{(k)}} \cdot \boldsymbol{u}_i^{(k)} = -\left(\boldsymbol{u}_i^{(k)}\right)^{\mathrm{T}} \cdot \int_Y \boldsymbol{B}_{\mathrm{e}}^T \frac{\partial \boldsymbol{D}_i^{(k)}}{\partial \bar{\rho}_i^{(k)}} \boldsymbol{B}_{\mathrm{e}} \mathrm{d}Y \cdot \boldsymbol{u}_i^{(k)} \tag{21}$$

In this paper, the effective elasticity matrix $\boldsymbol{D}_i^{H(k)}$ is pre-fitted as a function with the element density $\bar{\rho}_i^{(k)}$, so $\partial \boldsymbol{D}_i^{(k)}/\partial \bar{\rho}_i^{(k)}$ can be acquired, and further gives $\partial c^{(k)}/\partial \bar{\rho}_i^{(k)}$. Simplifying damage of the microstructure enables easier calculation of $\boldsymbol{D}_i^{H(k)}$, more details will be described in Section 5.3.

For SIMP, the compliance of element i and its sensitivity are obtained by the following two equations:

$$c_i^{(k)} = E\left(\bar{\rho}_i^{(k)}\right)\left(\boldsymbol{u}_i^{(k)}\right)^{\mathrm{T}} \boldsymbol{K}_0 \boldsymbol{u}_i^{(k)} = \left[\left(\bar{\rho}_i^{(k)}\right)^p (E_0 - E_{min}) + E_{min}\right]\left(\boldsymbol{u}_i^{(k)}\right)^{\mathrm{T}} \boldsymbol{K}_0 \boldsymbol{u}_i^{(k)} \tag{22}$$

$$\frac{\partial c^{(k)}}{\partial \bar{\rho}_i^{(k)}} = \frac{\partial c_i^{(k)}}{\partial \bar{\rho}_i^{(k)}} = -p\left(\bar{\rho}_i^{(k)}\right)^{p-1} (E_0 - E_{min})\left(\boldsymbol{u}_i^{(k)}\right)^{\mathrm{T}} \boldsymbol{K}_0 \boldsymbol{u}_i^{(k)} \tag{23}$$

4.4. Objective function, volume constraint function and their sensitivities

After finding the compliance $c^{(k)}$ under each failure scenario, the objective function $\bar{J}$ can be derived from Eq. (2). The partial derivative of the objective function with respect to the compliance is:

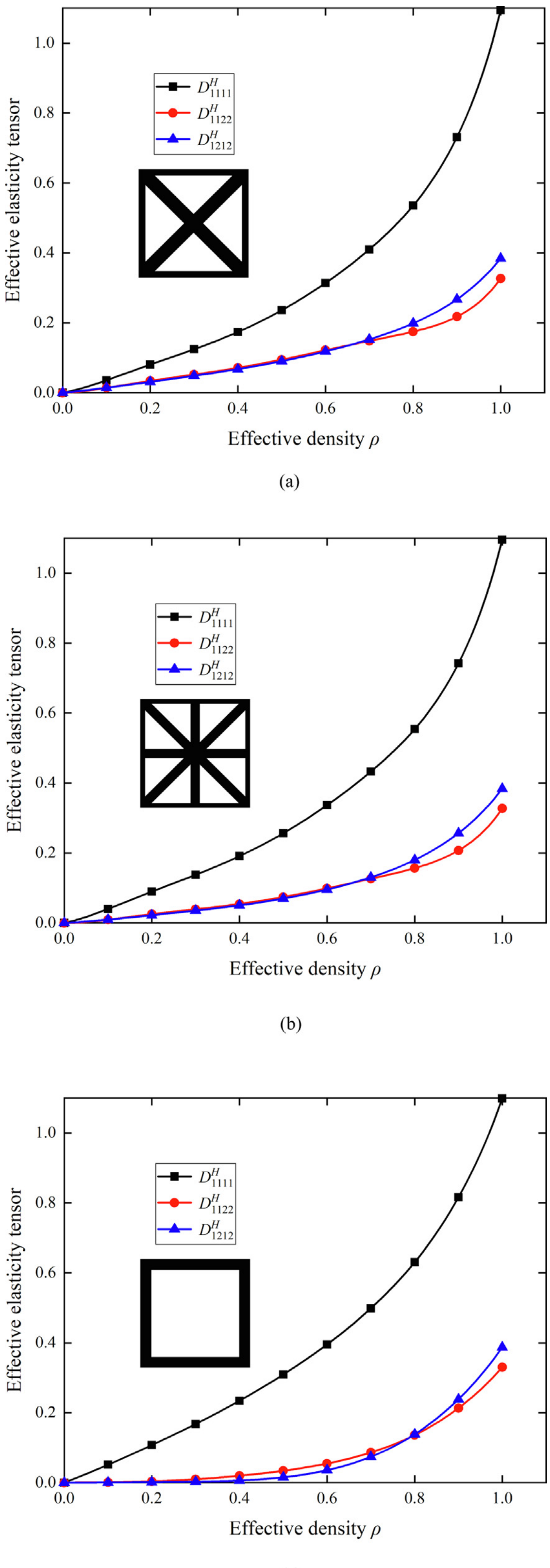

Fig. 4. The fitting curves of the effective elasticity tensors relative to the effective density for three microstructures: (a) material 1, (b) material 2 and (c) material 3.

$$\frac{\partial \bar{J}}{\partial c^{(k)}} = \frac{e^{\gamma c^{(k)}}}{\sum_{l=1}^{m} e^{\gamma c^{(l)}}} \tag{24}$$

Based on the sensitivities obtained above, the partial derivative of the objective function $\bar{J}$ with respect to the density of element i can be derived by the chain rule:

$$\frac{\partial \bar{J}}{\partial \rho_i} = \sum_{l=1}^{m} \sum_{h=1}^{n} \frac{\partial \bar{J}}{\partial c^{(l)}} \frac{\partial c^{(l)}}{\partial \bar{\rho}_h^{(l)}} \frac{\partial \bar{\rho}_h^{(l)}}{\partial \bar{\rho}_h} \frac{\partial \bar{\rho}_h}{\partial \tilde{\rho}_h} \frac{\partial \tilde{\rho}_h}{\partial \rho_i} \tag{25}$$

Assuming that the volume fraction is set to f_0, the volume constraint function is given by:

$$f(\boldsymbol{\rho}) = \frac{V(\boldsymbol{\rho})}{V_0} - f_0 = \frac{\sum_{h=1}^{n} v_h \bar{\rho}_h}{\sum_{h=1}^{n} v_h} - f_0 \leqslant 0 \tag{26}$$

Similarly, the sensitivity of the corresponding constraint function can be derived by the chain rule as follows:

$$\frac{\partial f}{\partial \rho_i} = \sum_{h=1}^{n} \frac{\partial f}{\partial \bar{\rho}_h} \frac{\partial \bar{\rho}_h}{\partial \tilde{\rho}_h} \frac{\partial \tilde{\rho}_h}{\partial \rho_i} \tag{27}$$

where $\partial f/\partial \bar{\rho}_i = v_i/\sum_{h=1}^{n} v_h$ can be obtained by Eq. (26).

4.5. Optimization procedure of MFSTO

The algorithm procedure of MFSTO is similar to FSTO for solid structures, the difference lies in the additional need to deal with microscale damage. The flow chart of MFSTO is shown in Fig. 3. As mentioned before, the effective elasticity matrix can be fitted as a function of the effective density to reduce the computational cost during the iteration, and the use of the simplified models reduces the difficulty of finding effective elasticity matrix.

5. Numerical examples

In this section, two 2D numerical examples and one 3D numerical example are employed to exhibit the superiority of optimized multiscale structures over optimized solid structures. All examples are computed on a desktop PC with CPU AMD core Ryzen 5 5600G of 3.90 GHz, RAM of 16 GB.

5.1. Parameters selection

For all examples, Young's modulus of the solid material is $E_0 = 1$ and Poisson's ratio is $v_0 = 0.3$. The penalty factor is equal to $p = 3$ in the SIMP method. The sizes of elements are 1×1 in 2D and $1 \times 1 \times 1$ in 3D, respectively.

To compare the design results of different microstructural configurations, three types of 2D microstructural unit cells are chosen in the most 2D examples whose effective elasticity matrices are calculated corresponding to relative densities. To ensure precision, all 2D microstructural cells are discretized into 500×500 quadrilateral linear finite elements. The damaged microstructure is usually anisotropic, and there can be up to 6 independent variables in the effective elasticity matrix. Therefore, to describe its properties more clearly, the effective elasticity tensors are selected for the function fitting. The fitting curves of the effective elasticity tensor relative to the effective density ρ are shown in Fig. 4, where the fitting functions fitted by the polynomial are listed in Table 1.

The effective elasticity matrices of the above microstructures have the same form:

$$\boldsymbol{D}^H = \begin{bmatrix} D^H_{1111} & D^H_{1122} & 0 \\ D^H_{1122} & D^H_{1111} & 0 \\ 0 & 0 & D^H_{1212} \end{bmatrix} \tag{28}$$

The 3D example is tested in Section 5.3 where the unit cell adopted is the ORC truss [39]. Fig. 5 shows schematic diagram of the ORC

Table 1
Effective elasticity tensor as a function of the effective density for three microstructures.

Material	Fitting function ($0 \leqslant \rho \leqslant 1$)
	$D^H_{1111} = 11.5135\rho^6 - 28.8100\rho^5 + 27.7130\rho^4 - 12.0338\rho^3 + 2.5087\rho^2 + 0.2026\rho$ $D^H_{1122} = 7.8853\rho^6 - 20.3870\rho^5 + 19.7592\rho^4 - 8.8001\rho^3 + 1.8445\rho^2 + 0.0250\rho$ $D^H_{1212} = 2.5097\rho^6 - 6.1442\rho^5 + 5.9397\rho^4 - 2.6068\rho^3 + 0.5800\rho^2 + 0.1056\rho$
	$D^H_{1111} = 12.1781\rho^6 - 30.5336\rho^5 + 29.2735\rho^4 - 12.6895\rho^3 + 2.6265\rho^2 + 0.2408\rho$ $D^H_{1122} = 7.5662\rho^6 - 19.6584\rho^5 + 19.2744\rho^4 - 8.6786\rho^3 + 1.8455\rho^2 - 0.0218\rho$ $D^H_{1212} = 2.0811\rho^6 - 5.1032\rho^5 + 5.1208\rho^4 - 2.3207\rho^3 + 0.5444\rho^2 + 0.0615\rho$
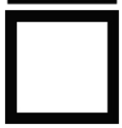	$D^H_{1111} = 2.4706\rho^6 - 4.9539\rho^5 + 4.1216\rho^4 - 1.4547\rho^3 + 0.4312\rho^2 + 0.4839\rho$ $D^H_{1122} = -0.7415\rho^6 + 2.7034\rho^5 - 2.9381\rho^4 + 1.4944\rho^3 - 0.2086\rho^2 + 0.0206\rho$ $D^H_{1122} = 0.6816\rho^4 - 0.3681\rho^3 + 0.0714\rho^2 - 0.0024\rho$

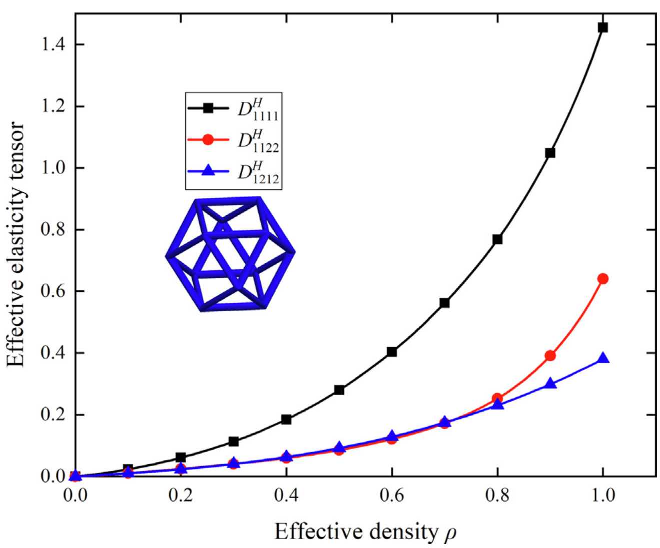

Fig. 5. The fitting curves of the effective elasticity tensors relative to the effective density for ORC truss.

truss and the fitting curve of its effective elasticity tensors relative to the effective density. These data are referenced to Watts et al. [40], and the fitting functions are displayed in Table 2.

Its effective elasticity matrix has the following form:

$$\boldsymbol{D}^H = \begin{bmatrix} D^H_{1111} & D^H_{1122} & D^H_{1122} & 0 & 0 & 0 \\ D^H_{1122} & D^H_{1111} & D^H_{1122} & 0 & 0 & 0 \\ D^H_{1122} & D^H_{1122} & D^H_{1111} & 0 & 0 & 0 \\ 0 & 0 & 0 & D^H_{1212} & 0 & 0 \\ 0 & 0 & 0 & 0 & D^H_{1212} & 0 \\ 0 & 0 & 0 & 0 & 0 & D^H_{1212} \end{bmatrix} \tag{29}$$

Table 2
Effective elasticity tensor as a function of the effective density for ORC truss.

Fitting function ($0 \leqslant \rho \leqslant 1$)
$D^H_{1111} = 1.4556\rho^6 - 3.4481\rho^5 + 2.7254\rho^4 + 0.0071\rho^3 + 0.4101\rho^2 + 0.1961\rho$
$D^H_{1122} = -2.7183\rho^6 + 6.3838\rho^5 - 4.4193\rho^4 + 1.2435\rho^3 - 0.0156\rho^2 + 0.1028\rho$
$D^H_{1212} = -1.5642\rho^6 + 3.5514\rho^5 - 2.6797\rho^4 + 0.9824\rho^3 - 0.0027\rho^2 + 0.0975\rho$

The same convergence criterion is adopted for all numerical examples: the iterations are stopped when the maximum change in the design variables is less than 1% or the number of iterations is more than 250. In Eq. (2), the value of γ is updated every 10 iterations or when the worst compliance changes rapidly. The filter radius $R_{\min}$ is set to 2 since a large $R_{\min}$ is unconducive to generating redundant trusses.

The parameter settings of the Heaviside projection have a considerable impact on the design results. To obtain better results, Heaviside projection is also applied to the multiscale TO. Taking material 1 in Fig. 4 and the cantilever beam model with a design domain size of 120×40 as an example, as the blue box shown in Fig. 6, damage will only appear in a 100×40 area on the left. The damage patch is a square area of 20×20, and the considered failure set is level 2. The global volume constraint is configured to 40%.

The projection threshold η is set to 0.5. Fig. 7 depicts the case where the initial value of the steepness parameter β is 2 and the termination value $\beta_{\max}$ are 0, 2, 4, 8, 16, and 32, respectively. Among them, $\beta_{\max} = 0$ means that the projection is not applied. The β value doubles every 50 iterations, the maximum number of iterations is 300 and the rest of the parameters are the same as above. It can be seen that if the projection is not applied or $\beta_{\max}$ is relatively small, the worst compliance $c_{\max}$ and the average compliance of all damage scenarios $\bar{c}$ may be higher. This is because the convergence speed is slow and the designs lack the necessary supporting structure. While $\beta_{\max}$ is relatively large, although the design is closer to the 0–1 distribution, $c_{\max}$ and $\bar{c}$ do not always decrease, and numerical instability may occur especially when $\beta_{\max}$ is larger than 16. It seems that an appropriate choice for $\beta_{\max}$ is 16, while the generated structure has better safety performance along with better convergence.

5.2. Example 1

Example 1 is derived from the work of Zhou and Fleury [15]. The boundary condition is shown in Fig. 8, with a global volume fraction of 20%. Damage can be applied to the entire design domain, but in order to prevent numerical instability, it is necessary to avoid applying load at void elements. That is, the damage needs to avoid the location where the load is applied. In this example, partial damage is not considered. The damage patches are set as 6×6 and 30×30 square areas, respectively, and the vertices of the damaged area coincide with the grid nodes to avoid damage inside the microstructural unit cell.

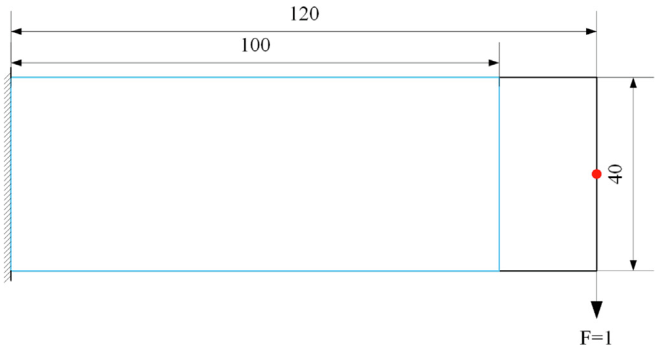

Fig. 6. Design domain and boundary condition of a cantilever beam.

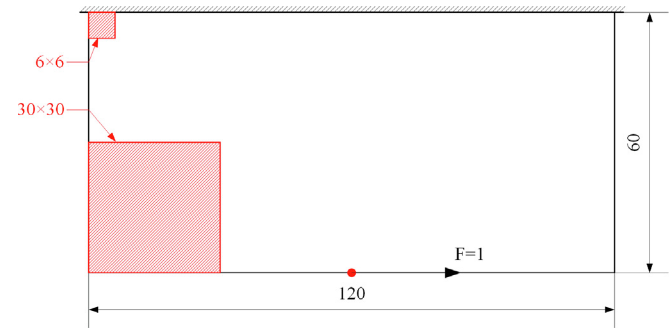

Fig. 8. Design domain and boundary condition of example 1.

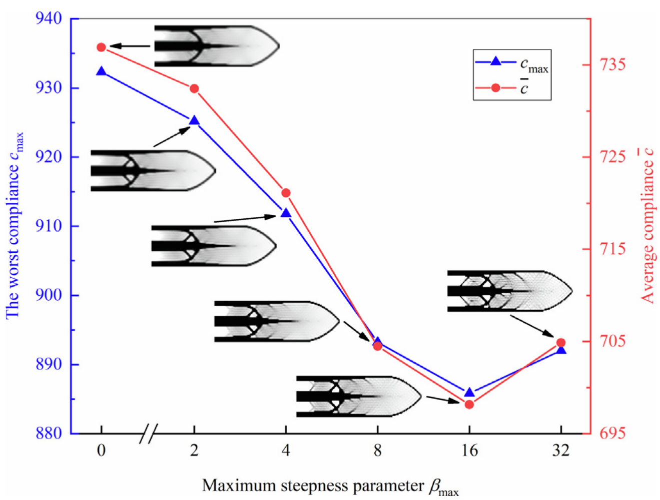

Fig. 7. Fail-safe designs and their compliances with different maximum steepness parameters β_{max}.

Performing deterministic TO according to the previous parameter settings, the obtained deterministic designs are shown in Fig. 9, whose configurations are two-force bars. Here, the design based on SIMP satisfies the convergence criterion at the 71st iteration. Lower β leads to more gray elements in SIMP design thus results in higher compliance.

The damage set is level 2. Since the damage is applied in the design domain except for the load point, the number of FEA to be calculated in each iteration is 744 for the 6×6 square damage, and 20 for the 30×30 square damage. The fail-safe designs of solid structures and multiscale structures are shown in Fig. 10, and the damage scenario that has the worst impact on structural compliance is marked with a red box. The compliance without considering damage c, the worst compliance c_{max} and the average compliance $\bar{c}$ are recorded in Table 3.

As can be seen from Fig. 10, the designs are related to the size of the damage patch. When the size is small, each fail-safe design resembles its deterministic design. When the size is larger, the designs based on solid and material 3 get clearer configurations. This is because their mechanical properties are poor in the intermediate density. While material 1 and 2 have better mechanical properties in the intermediate density, their fail-safe designs appear to have a large number of gray elements. In additions, $\beta_{max} = 16$ is not high enough to penalize designs based on material 1 and 2 into 0–1 distributions.

The small difference between the optimized designs of material 1 and material 2 indicates that the differences in the results in Table 3 are strongly related to the configuration of the microstructure. It can be also observed that the fail-safe designed multiscale

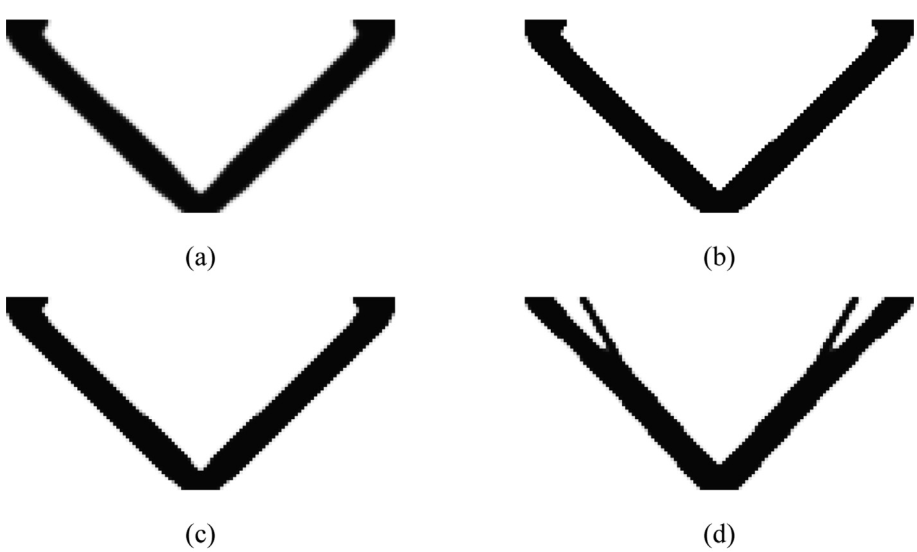

Fig. 9. Deterministic designs based on (a) SIMP, (b) material 1, (c) material 2 and (d) material 3 material models for example 1,and their compliances are $c = 12.2151$, $c = 11.5835$, $c = 11.7839$ and $c = 11.9726$, respectively.

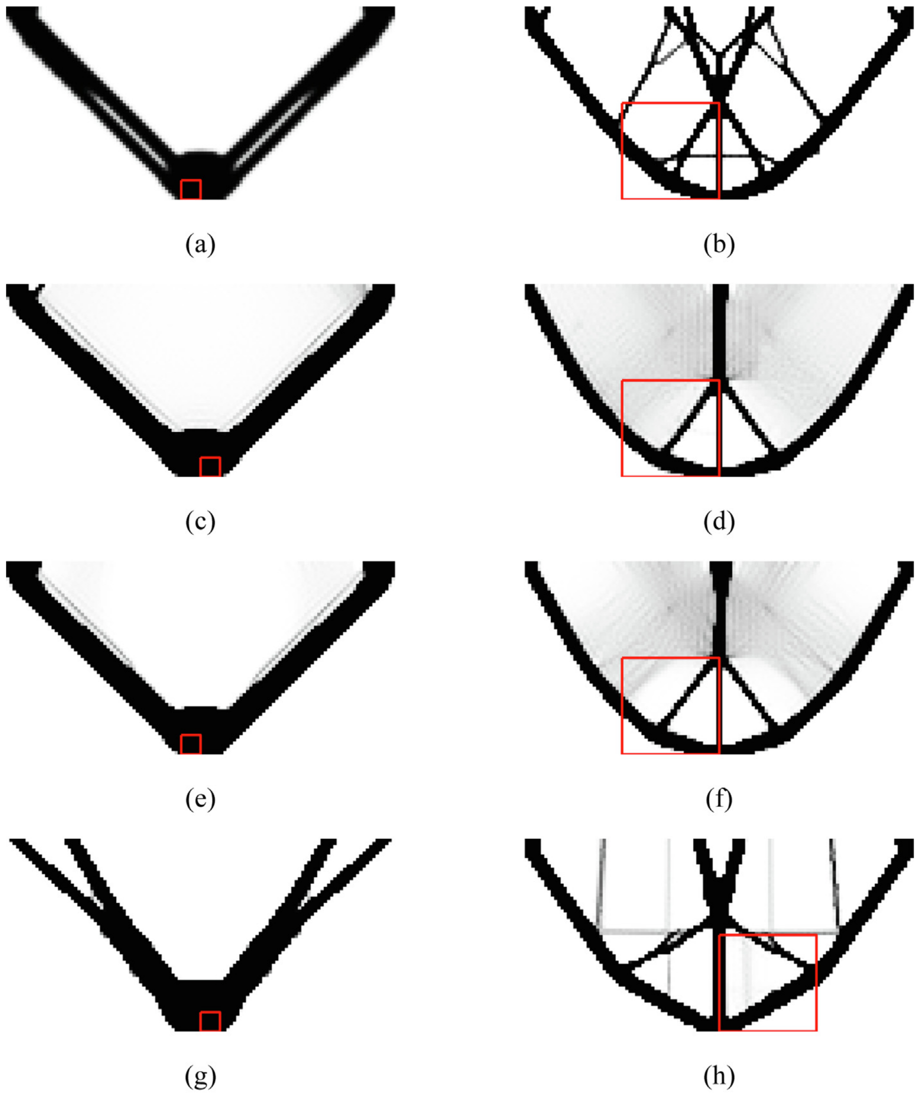

Fig. 10. Fail-safe designs based on (a,b) SIMP, (c,d) material 1, (e,f) material 2 and (g,h) material 3 material models for example 1, where the sizes of considering damage patches are 6×6 for the left and 30×30 for the right, respectively.

Table 3
Design results corresponding to Fig. 10.

	6×6			30×30		
	c	$c_{\max}$	$\bar{c}$	c	$c_{\max}$	$\bar{c}$
SIMP	13.2252	21.7832	14.1393	17.3453	40.5861	35.6764
Material 1	12.5479	20.8948	13.3035	19.0950	40.9721	34.0195
Material 2	12.5135	21.0054	13.3076	20.0744	41.3213	36.2382
Material 3	12.7726	20.6886	13.5207	19.7195	41.8938	38.4607

structure can have better mechanical properties than the solid structure, but it is related to the configuration of the microstructure.

Taking the fail-safe designs in Fig. 10(b)(d) as an example, their iteration curves are plotted in Fig. 11. The steepness parameter β doubles every 50 iterations, and the curves jump at these places. There are more gray elements in the design based on material 1, so more elements will be projected to 0 or 1, which causes the jumps to be much more drastic.

5.3. Example 2

Example 2 is a typical cantilever beam and its structural dimension and boundary condition are shown in Fig. 6, where the global volume constraint is set to 40%. The deterministic TO design is shown in Fig. 12. In this example, the material 3 based design is significantly different from the others and has higher compliance. This means that it may encounter the local optimization. Similar results were observed in [41].

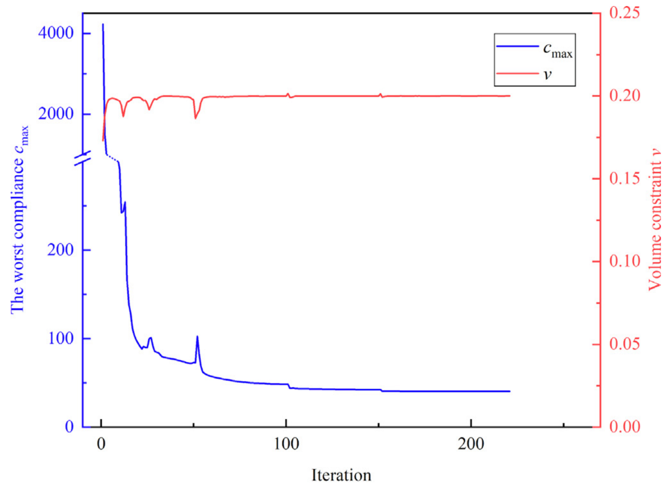

(a)

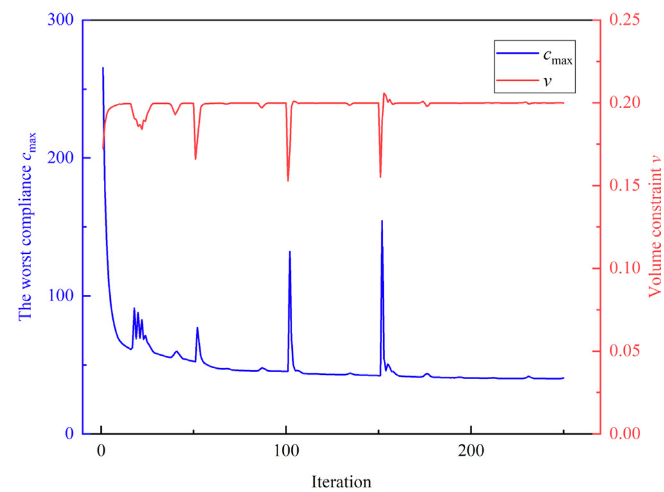

(b)

Fig. 11. The iteration curves corresponding to the designs in (a) Fig. 10(b) and (b) Fig. 10(d).

(a)

(b)

Fig. 13. Two different types of damage patches: (a) the shapes of the damage patches are square areas with 4×4 and 10×10; (b) the shapes of the damage patches are circular areas with radius $R = 1.3$ and 4.5.

Since microstructure elements may suffer partial damage, this example considers two different shapes of damage patches. As depicted in Fig. 13(a), the shape of the first type of damage patch is still a square, whose sizes will be set to 4×4 and 10×10, respectively. Partial damage of the microstructure is not considered at this moment. The shape of the second damage patch is chosen to be a circle, as depicted in Fig. 13(b), the center of which is located at the grid node while some microstructure elements will inevitably be partially damaged. The radius of the circular areas are fixed to $R = 1.3$ and 4.5, respectively, corresponding that elements in the range of 4×4 and 10×10 have suffered damage.

Considering the damage set of level 2, for 10×10 square damage and $R = 4.5$ circular damage, the number of FEA to be calculated in each iteration is 133; for 4×4 square damage and $R = 1.3$ circular damage, this number is 931.

For the two square damages shown in Fig. 13(a), the optimized designs and the locations of the worst damage are shown in Fig. 14. The compliance c, the worst-case compliance c_{max} and the average compliance $\bar{c}$ are recorded in Table 4.

By comparison, multiscale structures based on material 1 and 2 seem to be better suited to such boundary conditions, which show more robustness in this example. The diffuse gray elements improve the ability of multiscale structures to withstand damage, thus having lower c_{max} and $\bar{c}$.

(a)

(b)

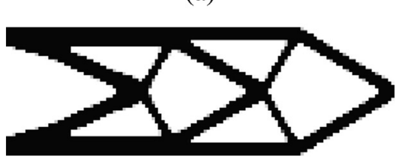

(c)

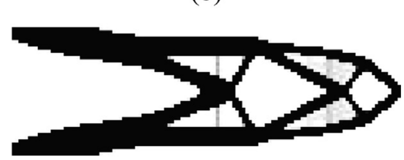

(d)

Fig. 12. Deterministic designs based on (a) SIMP, (b) material 1, (c) material 2 and (d) material 3 material models for example 2,and their compliances are $c = 203.6308$, $c = 203.2687$, $c = 203.0307$ and $c = 232.6615$, respectively.

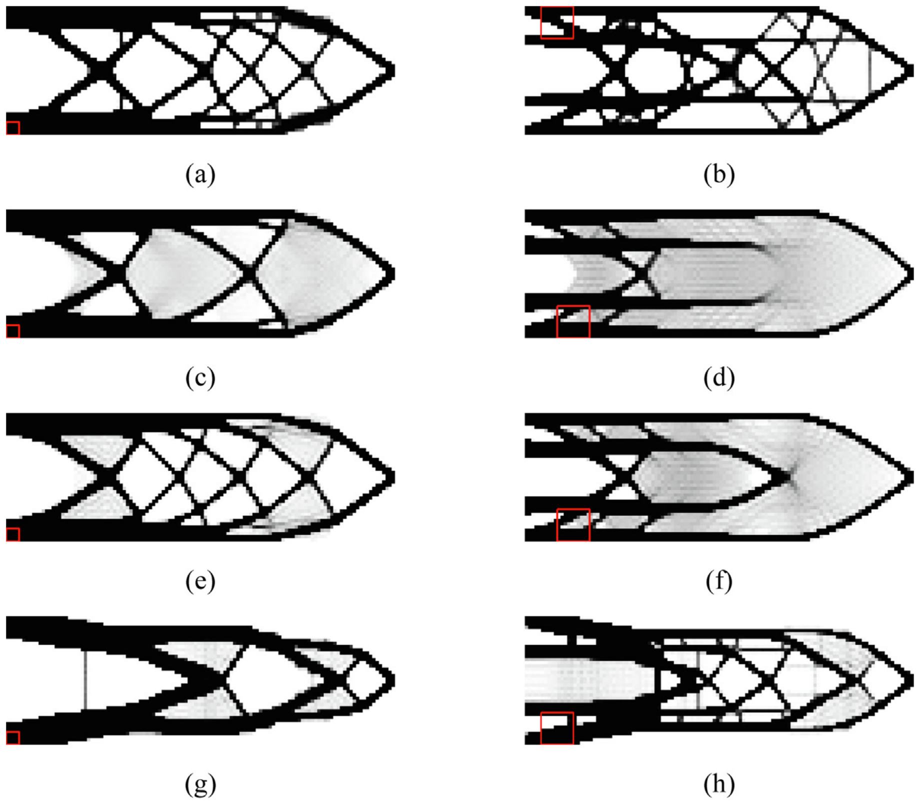

Fig. 14. Fail-safe designs based on (a,b) SIMP, (c,d) material 1, (e,f) material 2 and (g,h) material 3 material models for square damages shown in Fig. 13(a), where the sizes of considering damage patches are 4×4 for the left and 10×10 for the right, respectively.

Table 4
Results of fail-safe designs corresponding to Fig. 14 for square damages.

	4×4			10×10		
	c	$c_{\max}$	$\bar{c}$	c	$c_{\max}$	$\bar{c}$
SIMP	210.6999	254.6968	220.7133	266.8094	450.9851	345.7151
Material 1	212.6612	251.1608	219.4402	259.1313	408.2739	307.5418
Material 2	207.8138	245.6637	216.3276	261.5707	411.9660	318.2965
Material 3	239.8165	290.6256	247.3389	289.3638	455.4038	374.2881

However, the designs based on material 3 still fall into the local optimum, especially the design in Fig. 14(g). Take the density map and damage scenario of Fig. 14(a) as an example. The $c_{\max}$ of designs filled with material 1, 2, 3 are 252.8670, 255.4942, 254.9013, respectively. Because of this, material 3 will not be considered in the following example.

Furthermore, consider two damage patches shown in Fig. 13(b). For solid structures, the related sensitivity is easy to compute, so the accurate damaged models are employed during the optimization to improve the accuracy of the results. For multiscale structures, the simplified method shown in Fig. 1(b) is adopted for the partially damaged microstructural elements, that is, the trusses of the elements covered by the damaged area are removed. The simplified models adopted in this paper are shown in Fig. 15, where the rod diameter of the microstructural elements is 0.12 as examples and their effective elasticity matrices are given. For material 1, two types of simplified failure models are employed; for material 2, four types of simplified failure models are employed. The remaining failure models can be obtained by rotating or symmetric operations on such models. The worse performance of the simplified models will result in a more conservative design.

It should be pointed out that it is necessary to adopt simplified models. The main reason is that accurate models may be geometrically discontinuous due to the partial damage. Thus, the curves of the effective elasticity tensors relative to the effective density may have discontinuous first-order derivatives at these points. Choosing the proper simplified model can avoid this phenomenon. Taking a damaged element in the left of Fig. 15(a) and its corresponding simplified model as an example, the relation curves between their elasticity tensor D^H_{2222} and density are shown in Fig. 16. It can be seen that the derivative of the curve for the accurate model is discontinuous at the purple point where the geometric discontinuity occurred. It poses a challenge to its fitting and differentiating. Adopting the simplified model, on the other hand, can avoid this point.

The effective elasticity tensors of the simplified damaged cells also will be fitted by sextic polynomials. The designs of the solid structures and multiscale structures are shown in Fig. 17. To ensure the comparability of results, accurate damaged models will be adopted in the calculation with the results in Table 5. The worst damage cases are marked with red circles in Fig. 17.

The redundancy of the optimized structures depicted in Fig. 17 seems lower than that of the structures in Fig. 14 due to the

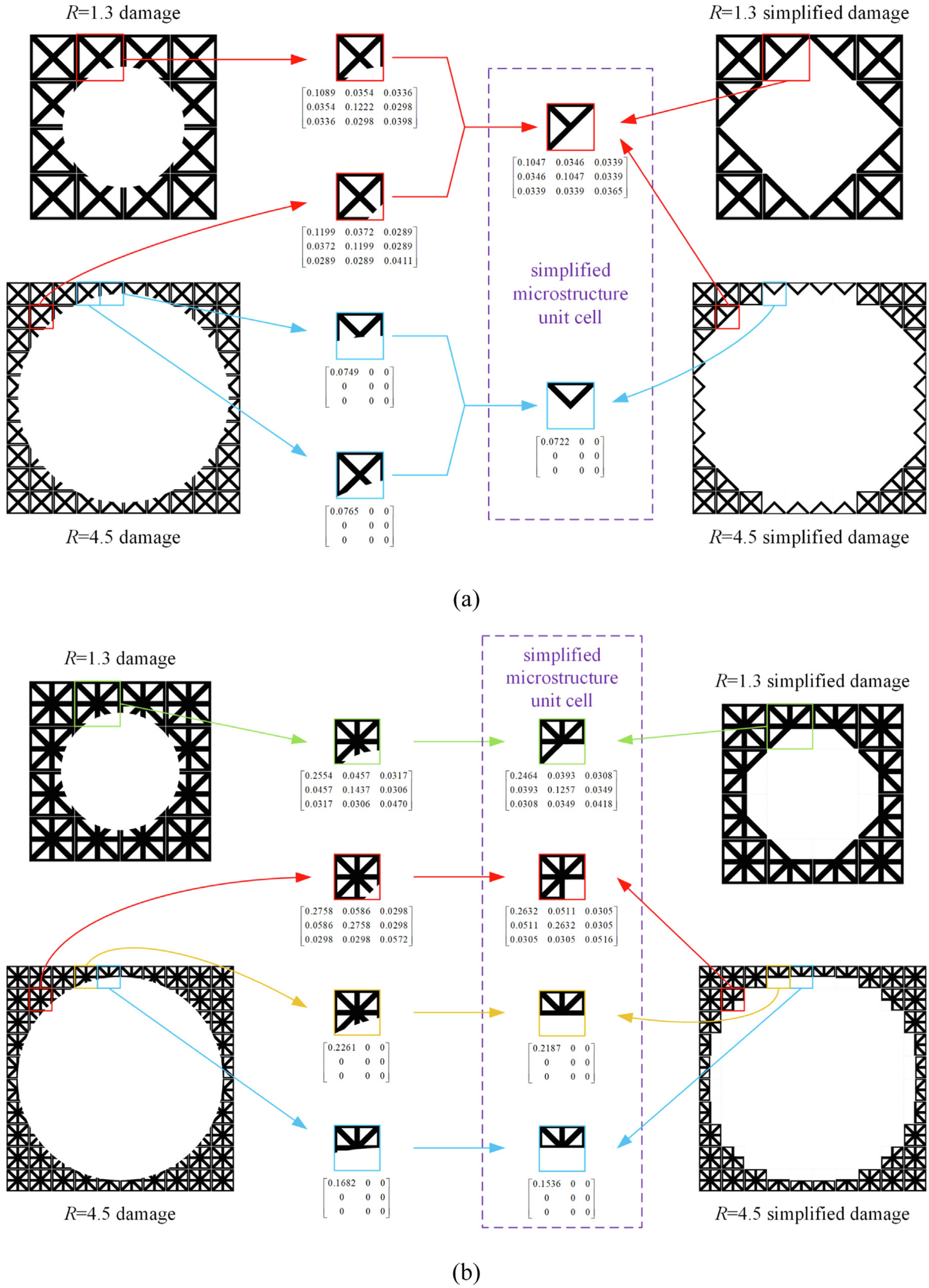

Fig. 15. The simplified models based on (a) material 1 and (b) material 2.

smaller area of the damage patches. The better performances of the multiscale optimized structures demonstrate the effectiveness of the aforementioned simplified approach, and also confirms the superiority of the multiscale structure. The higher redundancy of material 2 does not contribute much to reduce the c_{max} of the multiscale structure, but it can effectively reduce $\bar{c}$.

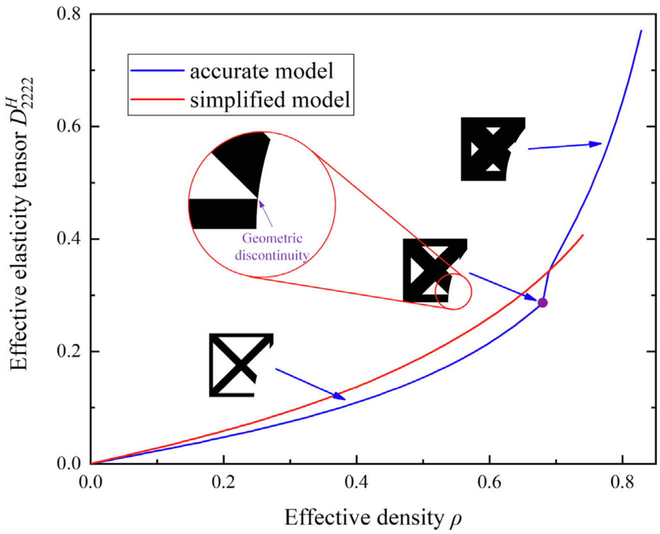

Fig. 16. The curves of the effective elasticity tensor D^H_{2222} relative to the effective density for accurate and simplified damaged model.

Combined with example 1, it can be seen that the performances of optimized multiscale structures are not always better than the optimized solid structure. There are two main reasons. First, the configuration of the microstructure may not “adapt” to the current constraints. Second, the multiscale designs may converge to local optimization.

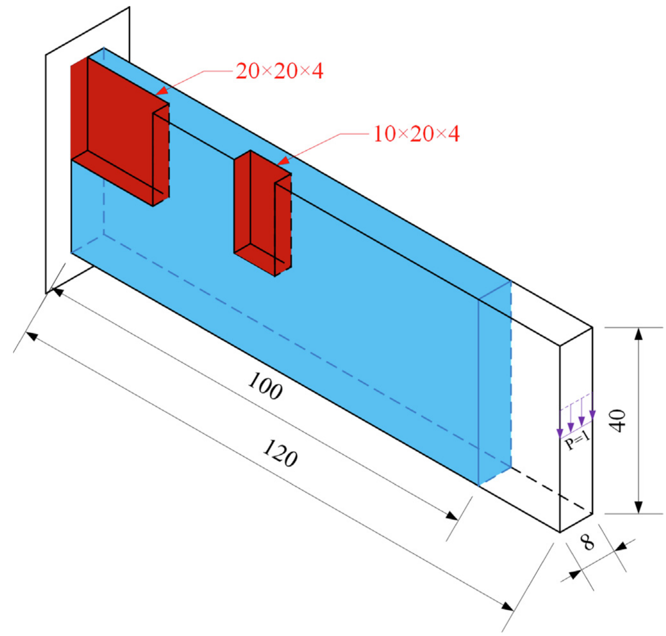

Fig. 18. Dimensions and boundary conditions for 3D cantilever beam example.

Through the above 2D numerical examples, it is not unreasonable to note that the optimized multiscale structures tend to generate a large number of gray elements, which not only increases the robustness, but also makes these gray regions

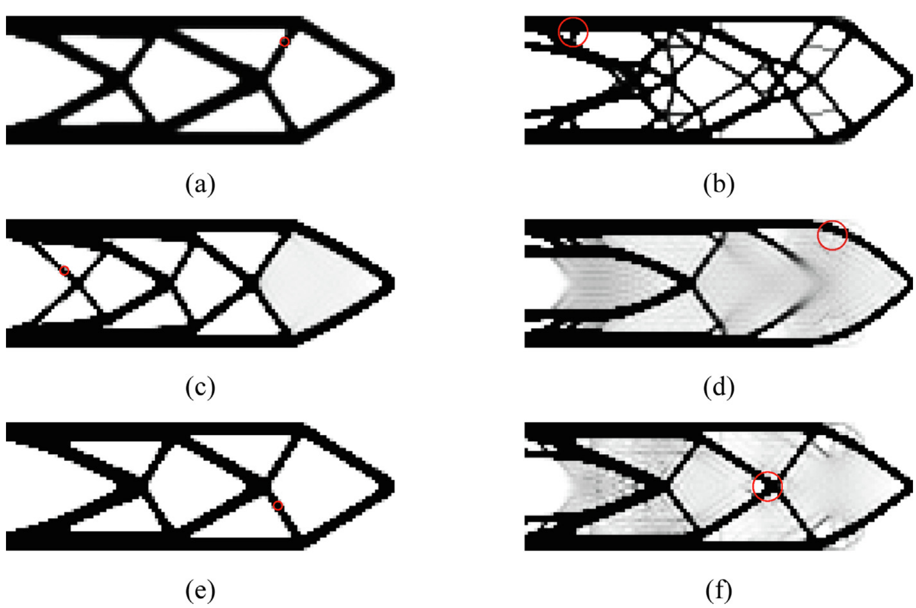

Fig. 17. Fail-safe designs based on (a,b) SIMP, (c,d) material 1 and (e,f) material 2 material models for circular damages shown in Fig. 13(b), where the radius of considering damage patches are $R = 1.3$ for the left and $R = 4.5$ for the right, respectively.

Table 5
Results of fail-safe designs corresponding to Fig. 17 for circular damages.

	$R = 1.3$			$R = 4.5$		
	c	$c_{\max}$	$\bar{c}$	c	$c_{\max}$	$\bar{c}$
SIMP	208.5945	218.8972	209.8703	230.0779	303.0931	260.7544
Material 1	203.9692	215.1473	205.3927	231.5120	288.8144	251.5018
Material 2	203.4005	211.6372	204.6170	224.3687	293.9973	246.8813

(a) (b)

Fig. 19. Deterministic designs based on (a) SIMP and (b) ORC truss material models for the 3D cantilever beam, and their compliances are $c = 3765.1494$ and $c = 3626.2229$, respectively.

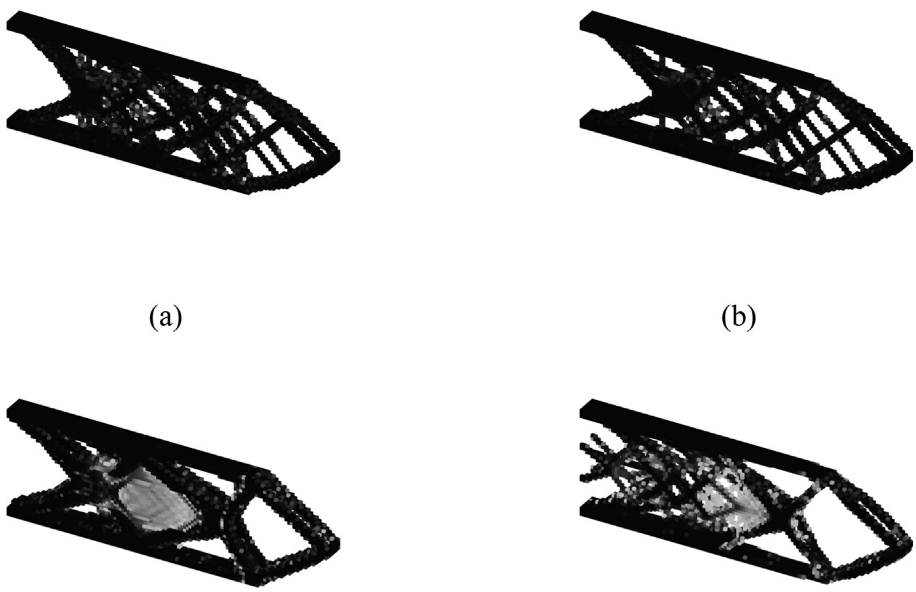

(a) (b)

(c) (d)

Fig. 20. Fail-safe designs based on (a,b) SIMP and (c,d) ORC truss material models for damages shown in Fig. 18, where the sizes of considering damage patches are $10 \times 20 \times 4$ for the left and $20 \times 20 \times 4$ for the right, respectively.

self-supporting. Generally, 45° is the minimum overhang angle that designs can be additive manufactured without support. There is a theory that a design can be printed without any support if its inclination angles of overhang portions are smaller than the minimum overhang angle. It was first implemented by Leary et al. [42]. Then, some researchers designed self-supporting structures by introducing overhang angle constraints into the optimization process [43–45]. There are many trusses with overhang angles less than 45° in the optimized solid structures, especially in example 2. In contrast, the multiscale structures are self-supporting in most regions filled with gray elements, and only requires additional support in some white regions (e.g., the left side of Fig. 17(d)). This brings convenience to its additive manufacturing.

5.4. Example 3

A 3D cantilever beam is used to demonstrate that the method can be extended to 3D cases. As shown in Fig. 18, the size of the cantilever beam is $120 \times 40 \times 8$. One end face is constrained, and a distributed vertical load with unit density is applied. Damage occurs in the light blue area shown in the figure with a size of $100 \times 40 \times 8$. The global volume fraction is set to 20%. Partial damage to the microstructure are not considered, and the damage patches are set to be cuboid regions with sizes of $20 \times 20 \times 4$ and $10 \times 20 \times 4$, respectively, as shown by the crimson cuboids in the figure.

The selection of other parameters is the same as that in Section 5.1, and the deterministic designs and results are obtained in Fig. 19, where elements with a density less than 0.2 are not shown. The ORC truss filled multiscale structure has lower compliance than the solid structure, and the fundamental reason is that the mechanical properties of the ORC truss are generally better than those of the material assumed by the SIMP method with the same density.

Still considering the damage set of level 2, for two damage cases of $20 \times 20 \times 4$ and $10 \times 20 \times 4$, 81 and 171 cases need to be calculated in each iteration, respectively. The fail-safe designs are shown in Fig. 20, and the design results are shown in Table 6.

Table 6
Results of fail-safe designs corresponding to Fig. 20.

	$10 \times 20 \times 4$			$20 \times 20 \times 4$		
	c	c_{max}	$\bar{c}$	c	c_{max}	$\bar{c}$
SIMP	3941.5818	4857.6131	4505.4999	3919.2830	5228.5781	4772.2955
ORC truss	3897.6228	4760.5423	4407.9432	4000.4665	5147.4381	4780.8244

Similar to the 2D case, in the 3D example, the ORC truss filled designs exist a large number of gray elements, which make structures redundant and self-supporting. Their c_{max} are lower than that of the solid optimized structure, but c and $\bar{c}$ are not always better. That is, the comprehensive performances of the optimized multiscale structures are not always better than that of the solid optimized structures. This shows the importance of the microstructural configuration to the results again.

6. Conclusions

In this paper, an implementation method of MFSTO is addressed. The partial damage of the microstructural element may need to be considered when the multiscale structure is damaged, which complicates the MFSTO. To facilitate the MFSTO problem, damage to the truss-like microstructure is simplified by removing the damaged bars, which makes the elasticity matrix and sensitivity easier to obtain.

The effective elasticity tensors of all microstructures are calculated via the HM. For reducing the computational cost, they will be solved in advance and then fitted to a polynomial function of the density. The sextic polynomial is chosen to maintain accuracy. Using these polynomials, the effective elasticity tensors of the microstructure with each density and the sensitivity can be obtained simply during the optimization process.

To gain clearer and superior designs, the filtering and the projection of variables are also applied to the MFSTO. The optimization problem is solved by the MMA solver. The K-S function is adopted to replace the non-derivable maximum function. The sensitivity related to failure can be obtained through the intermediate variable such as the rod diameter of the truss-like element.

Three numerical examples are listed in Section 5. The examples show that the multiscale optimized structures designed via the fail-safe theory can be more robust than the solid optimized structure, but it's strongly related to the configuration of the microstructure. Example 2 takes the partial damage of the microstructure into consideration, which proves the effectiveness of the simplified method. Example 3 extends the presented method to 3D for demonstrating the reliability of the algorithm. The results show that optimized multiscale structures, especially those that can accommodate larger damage, are filled with a large number of gray elements, which can support the entire structure. Moreover, these diffuse elements make optimized multiscale structures self-supporting in these areas and thus provide better manufacturability than optimized solid structures.

There is still some work to be done. The algorithm implemented in this paper is computationally expensive, so an efficient algorithm should be developed in the future (e.g., combine with GPU parallel [46], three-level mesh method [47], DOF reduction [48]). As mentioned above, the microstructural configuration has a great influence on the design results, and the best configuration needs to be found through fail-safe design. Therefore, applying the fail-safe concept to microstructure TO and concurrent TO should be also focused in future work.

Data availability

Data will be made available on request.

Declaration of Competing Interest

The authors declare that they have no known competing financial interests or personal relationships that could have appeared to influence the work reported in this paper.

Acknowledgment

This paper has been supported by National Natural Science Foundation of China [No. 52075184], Guangxi Science and Technology Plan and Project [No. 2021AC19131], Open-funding Project of State Key Laboratory of Digital Manufacturing Equipment and Technology (Huazhong University of Science and Technology) [No. DMETKF2021020]. These supports are gratefully acknowledged.

References

[1] Bendsøe MP, Kikuchi N. Generating optimal topologies in structural design using a homogenization method. Comput Meth Appl Mech Eng 1988;71:197–224. https://doi.org/10.1016/0045-7825(88)90086-2.
[2] Zhou M, Rozvany GIN. The COC algorithm, Part II: Topological, geometrical and generalized shape optimization. Comput Meth Appl Mech Eng Eng 1991;89:309–36. https://doi.org/10.1016/0045-7825(91)90046-9.
[3] Bendsøe MP, Sigmund O. Material interpolation schemes in topology optimization. Arch Appl Mech 1999;69:635–54. https://doi.org/10.1007/S004190050248.
[4] Sethian JA, Wiegmann A. Structural Boundary Design via Level Set and Immersed Interface Methods. J Comput Phys 2000;163:489–528. https://doi.org/10.1006/jcph.2000.6581.
[5] Wang MY, Wang X, Guo D. A level set method for structural topology optimization. Comput Meth Appl Mech Eng 2003;192:227–46. https://doi.org/10.1016/S0045-7825(02)00559-5.
[6] Guo X, Zhang W, Zhong W. Doing Topology Optimization Explicitly and Geometrically—A New Moving Morphable Components Based Framework. J Appl Mech 2014;81:081009. https://doi.org/10.1115/1.4027609.
[7] Zhang W, Yuan J, Zhang J, Guo X. A new topology optimization approach based on Moving Morphable Components (MMC) and the ersatz material model. Struct Multidiscip Optim 2016;53:1243–60. https://doi.org/10.1007/s00158-015-1372-3.
[8] Sun PF, Arora JS, Haug EJ. Fail-Safe Optimal Design of Structures. Eng Optimiz 1976;2:43–53. https://doi.org/10.1080/03052157608960596.
[9] Lüdeker JK, Kriegesmann B. Fail-safe optimization of beam structures. J Comput Des Eng 2019;6:260–8. https://doi.org/10.1016/j.jcde.2019.01.004.
[10] Mohr DP, Stein I, Matzies T, Knapek CA. Redundant robust topology optimization of truss. Optim Eng 2014;15:945–72. https://doi.org/10.1007/s11081-013-9241-7.
[11] Kanno Y. Redundancy Optimization of Finite-Dimensional Structures: Concept and Derivative-Free Algorithm. J Struct Eng 2017;143:04016151. https://doi.org/10.1061/(ASCE)ST.1943-541X.0001630.
[12] Stolpe M. Fail-safe truss topology optimization. Struct Multidiscip Optim 2019;60:1605–18. https://doi.org/10.1007/s00158-019-02295-7.
[13] Dou S, Stolpe M. Fail-safe optimization of tubular frame structures under stress and eigenfrequency requirements. Comput Struct 2022;258:106684. https://doi.org/10.1016/j.compstruc.2021.106684.
[14] Jansen M, Lombaert G, Schevenels M, Sigmund O. Topology optimization of fail-safe structures using a simplified local damage model. Struct Multidiscip Optim 2014;9:657–66. https://doi.org/10.1007/s00158-013-1001-y.
[15] Zhou M, Fleury R. Fail-safe topology optimization. Struct Multidiscip Optim 2016;54:1225–43. https://doi.org/10.1007/s00158-016-1507-1.
[16] O. Ambrozkiewicz B. Kriegesmann Adaptive Strategies for Fail-Safe Topology Optimization. EngOpt 2018 proceedings of the 6th international conference on

engineering optimization, Springer. 2019; 200-11. https://doi.org/10.1007/978-3-319-97773-7_199.
[17] Ambrozkiewicz O, Kriegesmann B. Density-based shape optimization for fail-safe design. J Comput Des Eng 2020;7:615–29. https://doi.org/10.1093/jcde/qwaa044.
[18] Hederberg H, Thore CJ. Topology optimization for fail-safe designs using moving morphable components as a representation of damage. Struct Multidiscip Optim 2021;64:2307–21. https://doi.org/10.1007/s00158-021-02984-2.
[19] Martínez-Frutos J, Ortigosa R. Robust topology optimization of continuum structures under uncertain partial collapses. Comput Struct 2021;257:106677. https://doi.org/10.1016/j.compstruc.2021.106677.
[20] De Biagi V. Structural behavior of a metallic truss under progressive damage. Int J Solids Struct 2016;82:56–64. https://doi.org/10.1016/j.ijsolstr.2015.12.016.
[21] Kang Z, Liu P, Li M. Topology optimization considering fracture mechanics behaviors at specified locations. Struct Multidiscip Optim 2017;55:1847–64. https://doi.org/10.1007/s00158-016-1623-y.
[22] Serafinska A, Özenç K, Kaliske M. A coupled approach of optimization, uncertainty analysis and configurational mechanics for a fail-safe design of structures. Int J Numer Methods Eng 2017;109:125–52. https://doi.org/10.1002/nme.5282.
[23] Wu C, Fang J, Zhou S, Zhang Z, Sun G, Steven GP, et al. A path-dependent level set topology optimization with fracture criterion. Comput Struct 2021;249:106515. https://doi.org/10.1016/j.compstruc.2021.106515.
[24] Lakes R. Foam Structures with a Negative Poisson's Ratio. Science 1987;235:1038–40. https://doi.org/10.1126/science.235.4792.1038.
[25] Bückmann T, Thiel M, Kadic M, Schittny R, Wegener M. An elasto-mechanical unfeelability cloak made of pentamode metamaterials. Nat Commun 2014;5:4130. https://doi.org/10.1038/ncomms5130.
[26] Zheng X, Lee H, Weisgraber TH, Shusteff M, DeOtte J, Duoss EB, et al. Ultralight, Ultrastiff Mechanical Metamaterials. Science 2014;344:1373–7. https://doi.org/10.1126/science.1252291.
[27] Florijn B, Coulais C, van Hecke M. Programmable mechanical metamaterials. Phys Rev Lett 2014;113:175503. https://doi.org/10.1103/PhysRevLett.113.175503.
[28] Qiu Z, Li Q, Liu S, Xu R. Clustering-based concurrent topology optimization with macrostructure, components, and materials. Struct Multidiscip Optim 2021;63:1243–63. https://doi.org/10.1007/s00158-020-02755-5.
[29] Do QT, Nguyen CHP, Choi Y. Homogenization-based optimum design of additively manufactured Voronoi cellular structures. Addit Manuf 2021;45:102057. https://doi.org/10.1016/j.addma.2021.102057.
[30] Wu J, Aage N, Westermann R, Sigmund O. Infill Optimization for Additive Manufacturing-Approaching Bone-Like Porous Structures. IEEE Trans Vis Comput Graph 2018;24:1127–40. https://doi.org/10.1109/TVCG.2017.2655523.
[31] Liu L, Yan J, Cheng G. Optimum structure with homogeneous optimum truss-like material. Comput Struct 2008;86:1417–25. https://doi.org/10.1016/j.compstruc.2007.04.030.
[32] Sigmund O. Materials with prescribed constitutive parameters: An inverse homogenization problem. Int J Solids Struct 1994;31:2313–29. https://doi.org/10.1016/0020-7683(94)90154-6.
[33] Kreisselmeier G, Steinhauser R. Application of vector performance optimization to a robust control loop design for a fighter aircraft. Int J Control 1983;37:251–84. https://doi.org/10.1080/00207179.1983.9753066.
[34] Sigmund O, Maute K. Topology optimization approaches. Struct Multidiscip Optim 2013;48:1031–55. https://doi.org/10.1007/s00158-013-0978-6.
[35] Svanberg K. The method of moving asymptotes-A new method for structural optimization. Int J Numer Methods Eng 1987;24:359–73. https://doi.org/10.1002/nme.1620240207.
[36] Svanberg K. A Class of Globally Convergent Optimization Methods Based on Conservative Convex Separable Approximations. SIAM J Optim 2002;45:555–73. https://doi.org/10.1137/S1052623499362822.
[37] Sigmund O. Morphology-based black and white filters for topology optimization. Struct Multidiscip Optim 2007;33:401–24. https://doi.org/10.1007/s00158-006-0087-x.
[38] Wang F, Lazarov BS, Sigmund O. On projection methods, convergence and robust formulations in topology optimization. Struct Multidiscip Optim 2011;43:767–84. https://doi.org/10.1007/s00158-010-0602-y.
[39] Watts S, Tortorelli DA. A geometric projection method for designing three-dimensional open lattices with inverse homogenization. Int J Numer Methods Eng 2017;112:1564–88. https://doi.org/10.1002/nme.5569.
[40] Watts S, Arrighi W, Kudo J, Tortorelli DA, White DA. Simple, accurate surrogate models of the elastic response of three-dimensional open truss micro-architectures with applications to multiscale topology design. Struct Multidiscip Optim 2019;60:1887–920. https://doi.org/10.1007/s00158-019-02297-5.
[41] Wu J, Sigmund O, Groen JP. Topology optimization of multi-scale structures: a review. Struct Multidiscip Optim 2021;63:1455–80. https://doi.org/10.1007/s00158-021-02881-8.
[42] Leary M, Merli L, Torti F, Mazur M, Brandt M. Optimal topology for additive manufacture: A method for enabling additive manufacture of support-free optimal structures. Mater Des 2014;63:678–90. https://doi.org/10.1016/j.matdes.2014.06.015.
[43] Gaynor AT, Guest JK. Topology optimization considering overhang constraints: Eliminating sacrificial support material in additive manufacturing through design. Struct Multidiscip Optim 2016;54:1157–72. https://doi.org/10.1007/s00158-016-1551-x.
[44] Johnson TE, Gaynor AT. Three-dimensional projection-based topology optimization for prescribed-angle self-supporting additively manufactured structures. Addit Manuf 2018;24:667–86. https://doi.org/10.1016/j.addma.2018.06.011.
[45] Zhang W, Wang C, Zhou L, Gao T. Three-dimensional topology optimization considering overhang constraints with B-spline parameterization. Comput Struct 2022;269:106823. https://doi.org/10.1016/j.compstruc.2022.106823.
[46] Schmidt S, Schulz V. A 2589 line topology optimization code written for the graphics card. Comput Visual Sci 2012;14:249–56. https://doi.org/10.1007/s00791-012-0180-1.
[47] Wang Y, Zheng W, Zheng Y, Da D. A new three-level mesh method to accelerate the structural topology optimization. Appl Math Model 2022;109:374–400. https://doi.org/10.1016/j.apm.2022.05.012.
[48] Zheng W, Wang Y, Zheng Y, Da D. Efficient topology optimization based on DOF reduction and convergence acceleration methods. Adv Eng Softw 2020;149:102890. https://doi.org/10.1016/j.advengsoft.2020.102890.